ACS Photonics

pubs.acs.org/journal/apchd5

Article

CMOS-Compatible Bias-Tunable Dual-Band Detector Based on GeSn/Ge/Si Coupled Photodiodes

Enrico Talamas Simola,* Vivien Kiyek, Andrea Ballabio, Viktoria Schlykow, Jacopo Frigerio, Carlo Zucchetti, Andrea De Iacovo, Lorenzo Colace, Yuji Yamamoto, Giovanni Capellini, Detlev Grützmacher, Dan Buca,* and Giovanni Isella

Cite This: *ACS Photonics* 2021, 8, 2166−2173

Read Online

ACCESS | Metrics & More | Article Recommendations | Supporting Information

ABSTRACT: Infrared (IR) multispectral detection is attracting increasing interest with the rising demand for high spectral sensitivity, room temperature operation, CMOS-compatible devices. Here, we present a two-terminal dual-band detector, which provides a bias-switchable spectral response in two distinct IR bands. The device is obtained from a vertical GeSn/Ge/Si stack, forming a double junction *n-i-p-i-n* structure, epitaxially grown on a Si wafer. The photoresponse can be switched by inverting the bias polarity between the near and the short-wave IR bands, with specific detectivities of 1.9×10^{10} and 4.0×10^{9} cm·(Hz)$^{1/2}$/W, respectively. The possibility of detecting two spectral bands with the same pixel opens up interesting applications in the field of IR imaging and material recognition, as shown in a solvent detection test. The continuous voltage tuning, combined with the nonlinear photoresponse of the detector, enables a novel approach to spectral analysis, demonstrated by identifying the wavelength of a monochromatic beam.

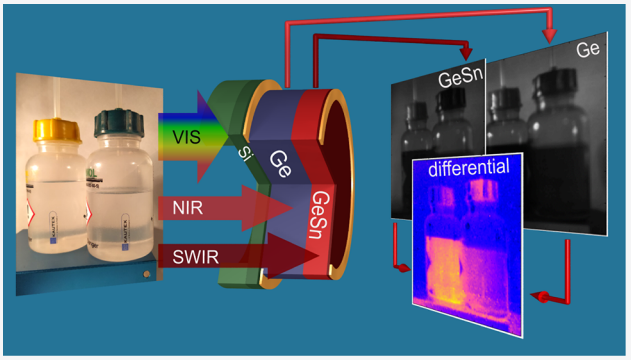

KEYWORDS: *GeSn, Ge-on-Si, dual-band photodetector, infrared imaging*

The development of optical devices operating in the near-infrared (NIR: λ = 750−1400 nm) and short-wave infrared (SWIR, λ = 1400−2500 nm) spectral ranges is experiencing a strong renaissance driven by Internet of Things (IoT) and Artificial Intelligence of Things (AIoT) applications.[1,2] These regions of the electromagnetic spectrum provide a wealth of information not accessible to cameras operating in the visible range (VIS, λ = 380−750 nm), which is extremely relevant for autonomous driving, security, medical, and environmental monitoring applications.[3−5] Since Rayleigh scattering on small particles is proportional to λ^{-4}, when compared to VIS, SWIR features longer penetration depths in high scattering media, such as rain, fog, or smoke, thus enabling enhanced visibility in severe weather conditions, estimation of distance and localization of obstacles.[6] Improving the current machine vision systems is of critical importance for aircraft landing, drone inspection, and self-driving cars.[7,8] In addition, many materials and solvents are opaque under VIS illumination, but transparent in the SWIR range or, on the contrary, they are transparent in the VIS but feature intense absorption bands in the SWIR.

Few material systems are established for sensing the VIS and IR. While silicon (Si)-based image sensors dominate applications in the VIS and part of the NIR, III−V and II−VI semiconductors, like InGaAs, InSb, or HgCdTe (MCT) are used for SWIR imaging.[9] However, such material systems suffer from a less mature technology when compared to Si, which complicates the integration with the read-out circuit. Solutions compatible with Si-based technology are, therefore, highly desirable. In this framework, new light sources[10−12] and detection devices[13] based on group IV germanium−tin (GeSn) semiconductors have emerged as solutions for NIR-SWIR applications.[14,15] The combination of Si, Ge, and Sn strongly widens the spectral range of operation, offering advanced architecture engineering and leveraging on the power of mature Si epitaxy and technology.[16,17]

In this article we present a dual-band GeSn/Ge/Si sensor obtained by the vertical integration of two *p-i-n* photodiodes. The back-to-back photodiode architecture was originally proposed for simple simultaneous demultiplexing/detection of two wavelengths.[18] Different versions of the idea followed using III−V,[19−22] II−VI,[23] and colloidal quantum dots based

Received: April 22, 2021
Published: July 12, 2021

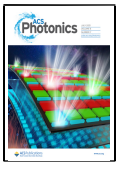

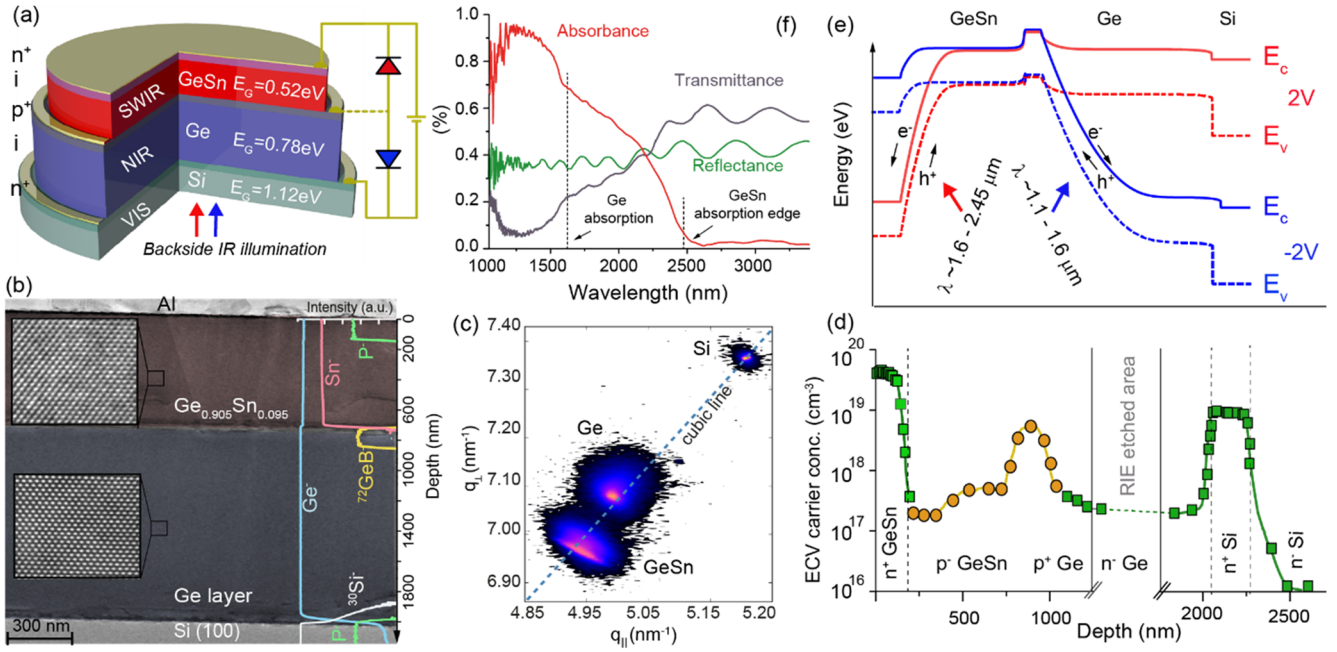

Figure 1. Material characterization: (a) Schematics of the vertical *n-i-p-i-n* double diode and working principle. (b) TEM image of the GeSn/Ge/Si stack and HR-TEM on individual GeSn and Ge layers. The overlapped SIMS elemental profiles highlight the contact doped regions. (c) RSM of the GeSn/Ge/Si heterostructure. (d) Depth distribution of electrically active dopants by ECV profiling. (e) Computed energy band structure at ±2 V applied bias, on the same scale as (d). The photocarriers flux created under NIR and SWIR light are indicated. (f) Absorbance of the GeSn/Ge heterostructure obtained by transmission/reflectance measurements. The Ge and GeSn absorption edges are marked.

materials,[24] yet the addressed optical region was mid to long IR ($\lambda > 4$ μm) or VIS-NIR as for a SiGe/Si or Ge/Si dual-band photodetector.[25,26] The spectral response for the hereby proposed dual-band GeSn/Ge/Si detector is tunable in the wavelength range between 1.05 and 2.45 μm (NIR-SWIR) by means of a simple change of the bias polarity.

The architecture of the device challenges traditional image sensors with a fixed spectral response, granting voltage-tunable operation over two distinct optical bands at the pixel level, thus providing self-aligned NIR/SWIR imagers. The ability to switch between NIR and SWIR, under identical illumination conditions, gives access to information that neither band can offer individually. We demonstrate the relevance and effectiveness of the approach through practical applications in IR imaging and spectrometry.

DEVICE STRUCTURE

The GeSn/Ge/Si device architecture comprises two vertically stacked GeSn/Ge and Ge/Si *n-i-p* photodiodes, monolithically integrated on a 200 mm Si wafer (Figure 1a). The heteroepitaxy is performed in industry-grade reduced pressure chemical vapor deposition (RP-CVD) systems.[27,28] The two photodiodes share the common p-type Ge layer, while the n-type GeSn and Si layers form the top and bottom contact, respectively. A positive (negative) voltage applied between the bottom and the top contact sets the GeSn/Ge diode in reverse (forward) bias and the Ge/Si diode in forward (reverse) bias, as shown in Figure 1a. By illuminating the photodetector through the polished backside of the Si substrate, which acts as an optical filter for VIS light, the electrical current flowing in the external circuit is generated within the reverse-biased diode, resulting in a tunable, dual-band photoresponse.

The Ge/Si photodiode consists of a 300 nm Si layer, n-type doped with phosphorus (P) to a concentration of 1×10^{19} cm^{-3}, followed by a 1 μm thick intrinsic Ge layer. The Ge epitaxy ends with a 100 nm boron (B)-doped Ge region with a concentration of 4×10^{18} cm^{-3}. The GeSn optically active region is 700 nm thick, with a Sn content of 9.5 at. %. The top contact is a 150 nm thick P-doped GeSn layer with a concentration of 2×10^{19} cm^{-3}. The high quality of the heterostructure is demonstrated by the cross-section transmission electron micrograph (TEM) of the heterostructure and the high resolution TEM insets shown in Figure 1b. The elemental distribution, given by secondary-ion mass spectrometry (SIMS), underlines the excellent interfaces and doping control (inset overlayed on the TEM). The interdiffusion at the Ge/Si interface arises during the cyclic thermal treatment performed to reach a low defect density in the Ge layer.[29] The lattice strain of the individual GeSn and Ge layers was extracted from high resolution X-ray diffraction (HR-XRD) reciprocal space mapping (RSM) (Figure 1c). The Ge layer is biaxially tensely strained, $\varepsilon_{||} = +0.17$, while the GeSn layer has a residual compressive strain of $\varepsilon_{||} = -0.21\%$. The distribution of electrically active dopants was profiled by electrochemical capacitance–voltage measurements (ECV, Figure 1d) and confirmed by temperature-dependent Hall measurements (Figure S2, Supporting Information). A very good agreement is obtained between the spatial distribution of the dopants' profiles from SIMS, ECV, and the intended doping values. The small discrepancy observed in the B-doped region at the GeSn/Ge interface is attributed to the presence of acceptor-like states induced by the misfit and threading dislocations at the GeSn/Ge interface responsible for the plastic relaxation of the GeSn layer.

Relying on the experimentally measured material parameters, the energy band diagram is calculated and shown Figure 1e for a ±2 V bias. The $Ge_{0.905}Sn_{0.095}$ alloy is a direct bandgap semiconductor with the fundamental bandgap energy at the Γ-

https://doi.org/10.1021/acsphotonics.1c00617
ACS Photonics 2021, 8, 2166–2173

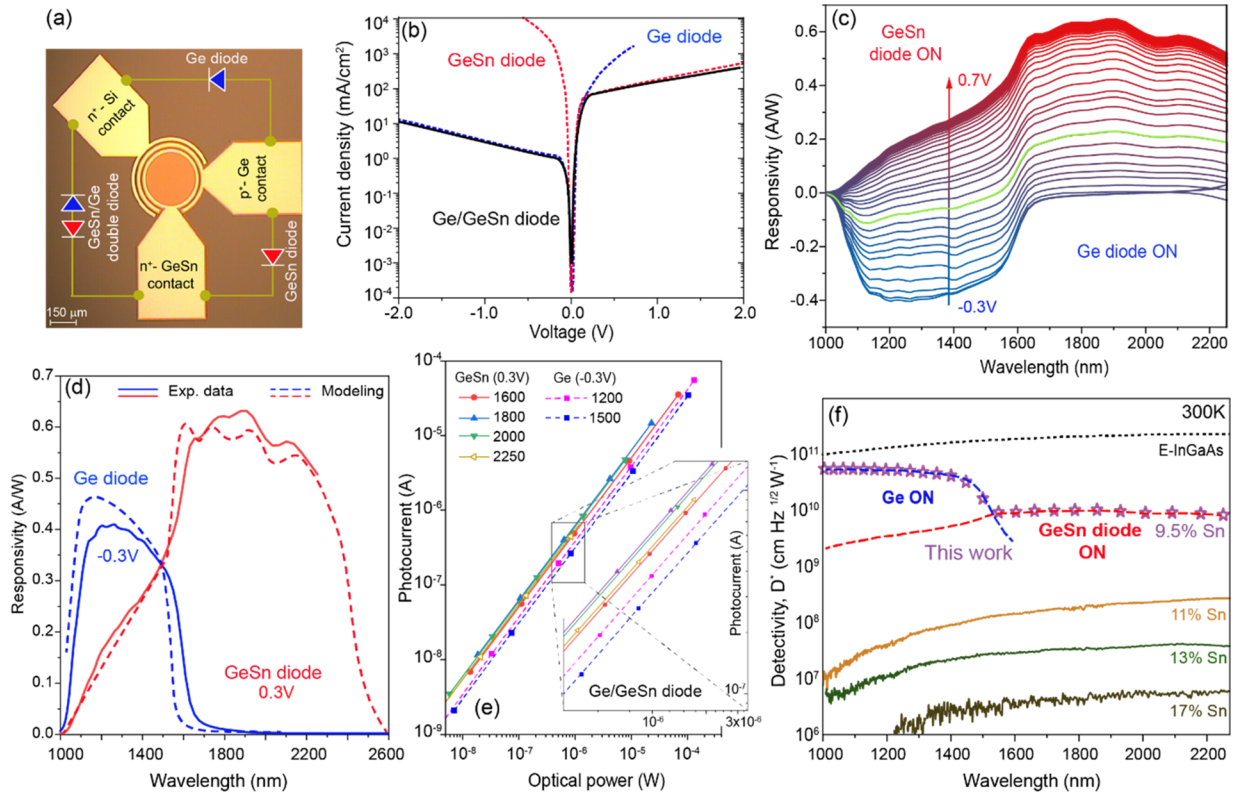

Figure 2. Opto-electrical characterization: (a) Optical image of a GeSn/Ge/Si dual-band device with three terminals for individual diodes characterization. (b) Dark current characteristics ($I-V$) of a 500 μm diameter GeSn/Ge/Si dual-band diode overlapped with the $I-V$ characteristics of GeSn/Ge and Ge/Si individual diodes measured as shown in (a). (c) Device responsivity, R, at different applied biases. (d) Experimental (full lines) and simulated (dashed lines) responsivities at ±0.3 V. (e) Log–log plot of the photocurrent vs optical power. (f) Wavelength-dependent detectivity, D^*, for a dual-band detector (star symbols) and its two components (red and blue dashed lines) measured as in (a). These data are benchmarked vs literature data[13] of single photodetectors at different Sn contents.

point of E_Γ = 0.50 eV, while the L-valleys are at the slightly higher energy of E_L = 0.55 eV. The tensile strained Ge is an indirect bandgap material with E_Γ = 0.78 eV and E_L = 0.66 eV, yet its optical absorption is dominated by the direct transition as shown by the absorbance of the GeSn/Ge epilayer obtained by combining reflectance and transmission measurements[30] (Figure 1f). The oscillatory pattern of reflectance and transmittance spectra are Fabry–Perot-like interferences due to multiple reflections in the Ge and GeSn layers.

DEVICE FABRICATION AND CHARACTERIZATION

Circular GeSn/Ge/Si voltage-tunable dual-band devices were fabricated using standard CMOS-compatible processing. A top view of a fabricated device is shown in Figure 2a. Some devices have an intermediate electrode contacting the p-type layer, allowing the individual characterization of the GeSn/Ge and Ge/Si photodiodes (see Supporting Information). Figure 2b shows the current–voltage ($I-V$) characteristic of a typical dual-band device, which is limited by the reverse bias currents of the Ge/Si diode at negative bias, and of the GeSn/Ge diode at positive bias. The typical dark current densities are 2.5 mA/cm^2 at −1 V and 135 mA/cm^2 at 1 V. These values compare well to state-of-the-art Ge-on-Si technology and to GeSn photodetectors with a similar Sn content.[13,31] III–V-based SWIR detectors typically feature lower dark currents,[32] yet the proposed devices would have a great impact in several applications with tight cost requirements.

The optical characterization was performed at room temperature using a tunable laser source (see Methods). The responsivity, $R = I_{ph}/P$, where I_{ph} is the photocurrent and P the incident optical power, measured for various applied biases ranging from −0.3 to 0.7 V, is presented in Figure 2c. The photoresponse is continuously tuned by the external bias: at a negative bias the detector operates in the NIR region, limited at lower wavelengths by the bandgap of the Si substrate, E_g-Si = 1.12 eV ∼ 1050 nm, and at longer wavelengths by the bandgap of the Ge layer, E_Γ-Ge = 0.78 eV ∼ 1600 nm. By switching to a positive bias the spectral response shifts to the SWIR region up to the GeSn bandgap, E_Γ-GeSn = 0.50 eV ∼ 2400 nm with the Ge layer acting as a low-pass optical filter. The laser source limited the device characterization to 2250 nm, shorter than the GeSn bandgap wavelength. An estimation of the GeSn diode cutoff wavelength can be seen in Figure 2d, where the experimentally measured responsivity is compared with that obtained by a drift-diffusion Poisson solver.[33] In this first demonstration of a GeSn/Ge/Si dual band photodetector, the Ge layer thickness (1 μm) is too thin to completely absorb the radiation at wavelengths below 1600 nm. This results in a partial overlap of the two diodes responsivities, as seen in Figure 2d. This issue could be overcome by increasing the Ge layer thickness to ≈2.5 μm, which is within the capability of industrial deposition tools. Peak responsivities of 0.41 A/W at 1200 nm and 0.64 A/W at 1900 nm are measured at the applied biases of −0.3 V and +0.3 V, respectively.

https://doi.org/10.1021/acsphotonics.1c00617
ACS Photonics 2021, 8, 2166–2173

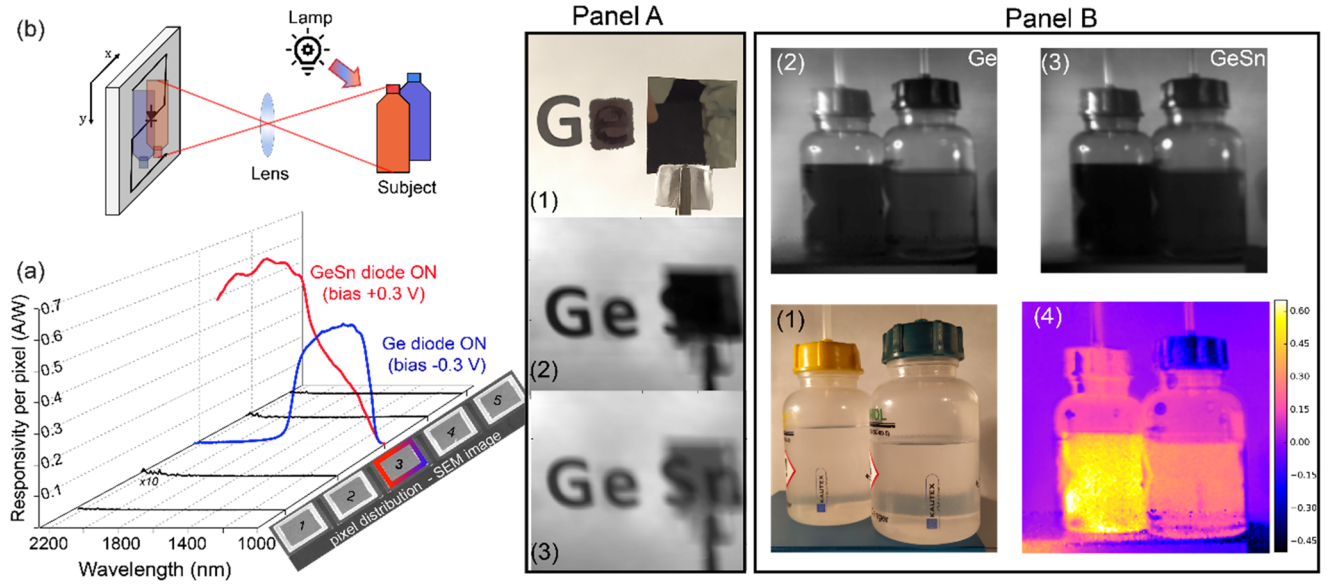

Figure 3. Imaging applications: (a) Responsivity of neighbor pixels 1, 2, 4, and 5, while the central one, pixel 3, is illuminated. (b) Sketch of the imaging single pixel rastering setup. Panel A: same scene viewed by (1) a VIS camera; and the dual-band GeSn/Ge device under applied bias (2) of −0.3 V, Ge/Si diode and (3) of +0.3 V, GeSn/Ge diode. Panel B: Differential imaging using the GeSn/Ge/Si dual-band device of two solvents. The color bar in panel B4 indicates, in arbitrary units, the contrast that a given pixel in the differential image has with respect to the background, used as a common reference level for the images taken with the Ge (panel B2) and GeSn (panel B3) detectors. Positive values indicate a stronger signal in the 1050−1600 nm band than in the 1600−2250 nm band, while an opposite behavior is obtained for negative values.

The photoresponse is tuned over a wide voltage range, yet most of the variation occurs near the crossover voltage ∼0.1 V, where the photocurrents generated by the two diodes equal out. Such a crossover voltage shows a weak dependence on the input optical spectrum. As can be seen in Figure 2c for $V = 0.1$ V, a negative photocurrent is obtained for $\lambda < 1550$ nm, while a positive photocurrent is observed at longer wavelengths; however, the bias range over which the photocurrent switches from negative to positive at some wavelength extends only for a few tens of mV around 0.1 V in the case of the hundreds of μW of optical power used in these experiments.

The responsivity saturates for an applied bias lower than −0.2 V and larger than +0.3 V, allowing a low-voltage operation, a relevant feature for low-power, integrated sensors. The photocurrent features a linear behavior, that is, a power-independent responsivity, over several orders of magnitude of input optical power (Figure 2e).

The overall performance of the detector is quantitatively evaluated by its specific detectivity, D^*, defined as $D^* = R\cdot(AB)^{1/2}/i_n$, where R is the responsivity, A is the device area, B is the bandwidth, and i_n is the noise current.[34] The specific detectivity is shown in Figure 2f. The Ge/Si photodiode's detectivity at −0.15 V is greater than 10^{10} cm·(Hz)$^{1/2}$/W in the 1100−1550 nm range, with a maximum of 2×10^{10} cm·(Hz)$^{1/2}$/W at 1200 nm. The GeSn/Ge diode detectivity at +0.25 V is above 3×10^9 cm·(Hz)$^{1/2}$/W in the 1600−2250 nm range, with a maximum of 4×10^9 cm·(Hz)$^{1/2}$/W at 1900 nm. The noise equivalent power (NEP) and external quantum efficiencies are reported in the Supporting Information.

Considering the strong dependence of D^* on the dark current density, a trade-off exists between detectivity and cutoff wavelength. By increasing the Sn content, the GeSn bandgap decreases, pushing the absorption band into the IR at the expense of an increased layer defectivity. The bandgap reduction and the lower crystal quality lead to a dark current increase and, consequently, to an overall reduction of D^*. This aspect is exemplified in Figure 2f, where the D^* of the present dual-band photodetector is compared to the literature data of single-band photodiodes operating in the NIR and SWIR regions.[13,35] The dual-band GeSn/Ge device presented here outperforms the detectivity of any literature reported GeSn single diode device with similar or larger Sn content. Larger detectivity values can be obtained, at the expenses of a shorter cutoff wavelength, by decreasing the Sn content.[36]

To probe the viability of the proposed detector as a dual-band NIR/SWIR imager, arrays composed of 5 square pixels have been fabricated to evaluate the optical cross-talk between pixels. Figure 3a displays the responsivity of different pixels while only the middle one (active pixel) is illuminated. The optical crosstalk, defined as $C = 20\cdot\log(I_{ac}/I_{in})$, where I_{ac} and I_{in} are the photocurrents of the active and inactive pixels, respectively, is ∼−50 dB throughout the whole spectrum for both positive and negative applied biases. The crosstalk can be improved by using antireflection layers, improving the Si wafer backside polishing and introducing light focusing on the pixels. These optimizations are beyond the scope of this work, but give clear pathways toward further development of the device.

To demonstrate the image acquisition capability, a simple raster-scanning system allowing for single-pixel imaging was used (see Methods). By switching the applied voltage between ±0.3 V, two images of the same subject are taken and compared to extract information unattainable from a single band image.

In Figure 3, Panel A, the text "GeSn", written with a common ink printer, is viewed using a VIS camera, and the dual-band GeSn/Ge detector. In the first case (A1) only the letter "G" is seen, while the ink covering the letter "e" is opaque in the VIS and the letters "Sn" are covered by a 1600 nm low-pass filter. A negative bias of −0.3 V activates the Ge detector, making the letter "e" readable (A2), while the remaining part of the text stays invisible. Switching the bias to +0.3 V activates

https://doi.org/10.1021/acsphotonics.1c00617
ACS Photonics 2021, 8, 2166−2173

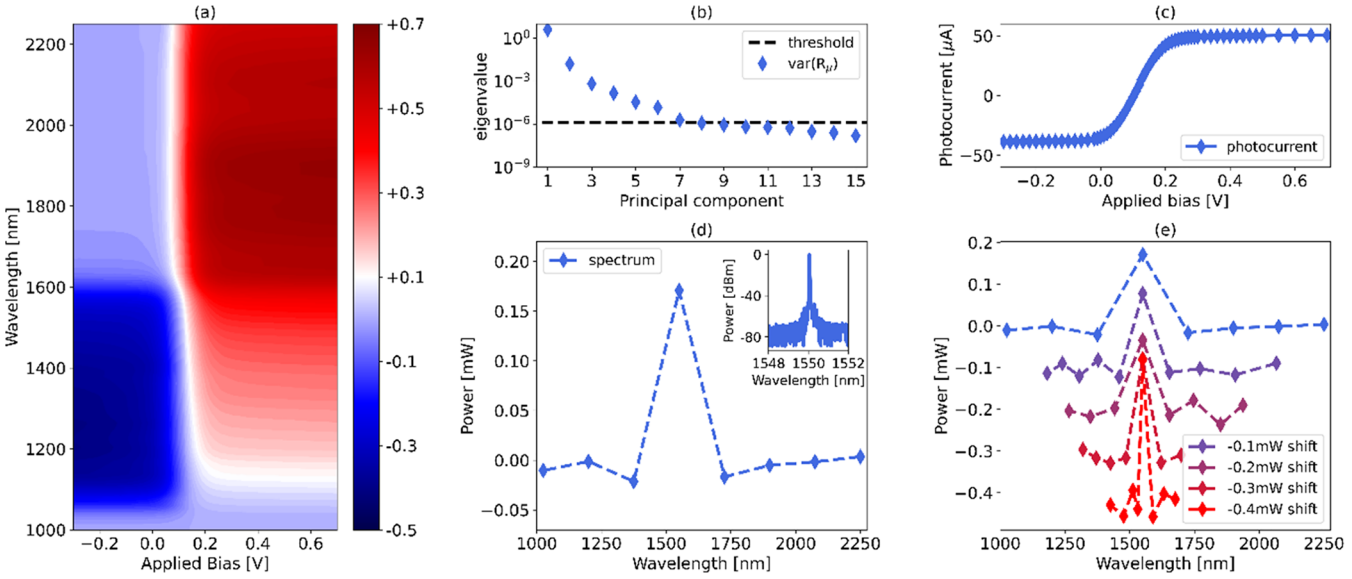

Figure 4. Spectrometry: (a) Contour plot of the responsivity matrix. (b) Eigenvalues of the covariance matrix of $\overline{\overline{R}}_{\mu}$ sorted in descending order (see Methods). The threshold corresponds to the first eigenvalue of the covariance matrix of $\overline{\overline{R}}_{\sigma}$ (see Methods). (c) Measured photocurrent at different bias voltages (see Methods). (d) Spectral reconstruction of the 1550 nm laser shown in the inset. (e) Sequence of spectral reconstructions targeting an iteratively smaller spectral range.

the GeSn diode and the complete text becomes readable (Panel A3). This example illustrates SWIR application in cultural heritage preservation, such as for subsurface examination of paintings or documents.[37]

Figure 3, Panel B, presents another application of the NIR-SWIR Ge/GeSn device employing differential imaging. The solvents in the vials, isopropanol and toluene, are transparent in the VIS spectral range (Panel B1), while they exhibit significant absorption in both NIR and SWIR regions, appearing somewhat opaque under Ge/GeSn device at −0.3 (B2) and +0.3 V (B3) with differences beyond easy eye recognition. However, performing a digital differential image (Supporting Information) allows distinguishing between the two solvents by exploiting their different degree of diffuse reflectance in the NIR and SWIR bands (B4).

The voltage-tunable GeSn/Ge/Si dual-band detector can also be exploited as an integrated solid-state spectrometer.[38] Indeed, the responsivity of the device depends not only on the wavelength λ, as is the case of conventional photodetectors, but also on the applied bias V. Given an array of voltages V_n and wavelengths λ_m, the responsivity can be conveniently represented as 2D matrix $\overline{\overline{R}}(V_m, \lambda_m)$. The illumination with an optical power $\overline{\overline{P}}(\lambda_m)$ will, therefore, lead to a voltage-dependent photocurrent:

$$\overline{I}_{\mathrm{ph}}(V_n) = \overline{\overline{R}}(V_n, \lambda_m)\overline{P}(\lambda_m) \tag{1}$$

By inverting eq 1, the optical spectrum $\overline{\overline{P}}(\lambda_m)$ can be retrieved from the photocurrent $\overline{I}_{\mathrm{ph}}(V_n)$, effectively operating the device as a spectrometer: the input power spectrum is recovered by calculating the matrix product between the inverse of the responsivity matrix and the array of the photocurrent measured at different voltages V_n:

$$\overline{P}(\lambda_m) = \overline{\overline{R}}^{-1}(V_n, \lambda_m)\overline{I}_{\mathrm{ph}}(V_n) \tag{2}$$

While the responsivity matrix is readily obtained by a set of dedicated calibration experiments (see Figure 4a), inverting *it* is a nontrivial problem which can be addressed through Moore−Penrose inverse and principal component analysis (PCA), as detailed in the Methods. For the device under investigation, PCA suggests that it is possible to distinguish up to eight relevant wavelengths between 1025 and 2250 nm, by measuring $\overline{I}_{\mathrm{ph}}(V_n)$ (Figure 4d) and performing the matrix product in eq 2.

Such a voltage-tunable spectrometer is tested by reconstructing the emission spectrum of a 1550 nm laser (inset of Figure 4d). The measured photocurrent as a function of the applied voltage, for an incident optical power of 130 μW, is shown in Figure 4c. Selecting eight equally spaced wavelengths, the reconstructed spectrum shown in Figure 4d is obtained. Although with a limited resolution, the device clearly identifies the correct wavelength of the laser. Assuming the absence of any significant power spectral density outside the reconstructed spectral window and exploiting the relative flatness of the responsivity matrix, arrays of wavelengths iteratively denser around 1550 nm are taken, improving the resolution within the part of the optical spectrum of interest (Figure 4e).

These imaging and spectrometry experiments demonstrate that dual-band GeSn/Ge/Si IR detectors can provide a step-change for multispectral imaging. The architecture of the proposed device combines at the pixel level operation over two IR bands, thus providing the straightforward acquisition of self-aligned NIR/SWIR images without the need of postprocessing. The GeSn/Ge/Si detector, based exclusively on group IV semiconductors, features excellent performance with figures of merit that are competitive with single band devices both in NIR and SWIR. Moreover, a relevant dark current reduction could be achieved by using thermoelectric coolers thus improving the performance. The demonstration of multiband imaging by scanning different subjects with a single-element detector and collecting both SWIR and NIR radiation shows the great potential of combining different spectral information for material identification and inspection.

With the encouraging multipixel device feasibility, addressed by optical crosstalk measurements, the integration with the

https://doi.org/10.1021/acsphotonics.1c00617
ACS Photonics 2021, 8, 2166−2173

read-out circuit can leverage on well-established Si-based electronics, making the manufacture of the GeSn/Ge/Si NIR-SWIR imagers in a Si-based foundry feasible.

METHODS

Epitaxial Growth. The material epitaxy was performed in two steps in separate industrial CVD reactors for 200 mm Si wafers. For the Si and Ge epitaxy an ASM Epsilon 2000 reduced pressure single wafer reactor was used and an Aixtron Tricent for the GeSn epitaxy. SiH_4 and GeH_4 are used as precursors for Si and Ge epitaxy and Ge_2H_6 and $SnCl_4$ for the GeSn epitaxy. In both reactors, B_2H_6 and PH_3 were used for p- and n-type doping. The specific epitaxial growth temperatures, 650 °C for Si, 550 °C for Ge, and 360 °C for GeSn, define the growth methodology in order to preserve the layer morphology and reduce the dopant diffusion. Consequently, the specific absorption band edges of the Ge and GeSn layers in the NIR-SWIR region defined the device illumination mode of operation, in this case the back side illumination.

Photocurrent Measurements. The optical characterization of the device was performed exploiting the monochromatized light of a supercontinuum laser (SuperK Extreme EXW-12, NKT Photonics). The light source can be tuned in the 1000−2250 nm wavelength range, with a typical half-width at half-maximum of 10 meV. The photocurrent is acquired by means of lock-in amplification. The optical power impinging on the device is measured in real time with a calibrated beam splitter and an InGaAs photodetector.

Single-Pixel Scanning Imaging System. The raster-scanning setup exploits a motor-controlled stage to take images using a single pixel. The subject is illuminated by a halogen lamp, while a N-BK7 plano convex lens projects its image on a plane that is scanned by the dual-band detector mounted on the motorized stage. Lock-in amplification is exploited to improve the signal-to-noise ratio. Finally, the image is reconstructed from the photocurrent acquired at each point of the scanning grid. The algorithm for the differential image shown in Figure 4, panel B-4, is detailed in the Supporting Information.

Matrix Inversion. $\overline{\overline{R}}$ is generally not square and is affected by random noise. While it is always possible to calculate the Moore−Penrose pseudoinverse of $\overline{\overline{R}}$, the unavoidable noise reduces the effective matrix rank, that is, the maximum number of independent columns or rows that can be effectively used for the spectral reconstruction.

To estimate such an effective rank, we propose the following procedure.

The responsivity matrix, composed of 62 voltages between −0.3 and +0.7 V and 70 wavelengths between 1 and 2.25 μm, has been measured five times, so that an average matrix $\overline{\overline{R}}_\mu$ (Figure 4a) and a standard deviation matrix $\overline{\overline{R}}_\sigma$ are obtained.

The $\overline{\overline{R}}_\mu$ matrix is then analyzed through PCA, considering the wavelengths as variables and the voltages as entries. PCA allows to recover the directions of maximum variance of the entries within the 70-dimensional space spanned by the variables. The 15 largest eigenvalues obtained from $\overline{\overline{R}}_\mu$ are shown in Figure 4b.

To determine the effective rank of $\overline{\overline{R}}$, we calculate the first principal component of $\overline{\overline{R}}_\sigma$ and use its eigenvalue as a threshold for the eigenvalues of $\overline{\overline{R}}_\mu$. This is also displayed in Figure 4b. The first eigenvalue of $\overline{\overline{R}}_\sigma$ is extremely close to the eighth eigenvalue of $\overline{\overline{R}}_\mu$, allowing us to estimate the effective rank of $\overline{\overline{R}}_\mu$ as 8.

Therefore, the dual-band device could realistically reconstruct up to eight different wavelengths from a photocurrent measurement obtained by applying a sweeping voltage.

Since the principal components are linear combinations of all 70 wavelengths, a spectral reconstruction on that base is rather worthless. The implemented procedure consists in choosing eight wavelengths and calculating the Moore−Penrose pseudoinverse of such a 62 × 8 matrix. Excluding the longest (and noisiest) wavelengths, despite reducing the total amount of "information" available, does lead to a higher effective matrix rank, allowing more wavelengths to be reconstructed. This is shown in the "−0.1 mW" reconstruction in Figure 4e.

ASSOCIATED CONTENT

Supporting Information

The Supporting Information is available free of charge at https://pubs.acs.org/doi/10.1021/acsphotonics.1c00617.

Experimental details and additional results (PDF)

AUTHOR INFORMATION

Corresponding Authors

Enrico Talamas Simola − *LNESS Dipartimento di Fisica, Politecnico di Milano, 22100 Como, Italy; Peter Grünberg Institute 9 (PGI-9) and JARA-Fundamentals of Future Information Technologies (JARA-FIT), Forschungszentrum Jülich, 52425 Jülich, Germany;* orcid.org/0000-0001-5468-6712; Email: enrico.talamas@polimi.it

Dan Buca − *Peter Grünberg Institute 9 (PGI-9) and JARA-Fundamentals of Future Information Technologies (JARA-FIT), Forschungszentrum Jülich, 52425 Jülich, Germany;* Email: d.m.buca@fz-juelich.de

Authors

Vivien Kiyek − *Peter Grünberg Institute 9 (PGI-9) and JARA-Fundamentals of Future Information Technologies (JARA-FIT), Forschungszentrum Jülich, 52425 Jülich, Germany*

Andrea Ballabio − *LNESS Dipartimento di Fisica, Politecnico di Milano, 22100 Como, Italy;* orcid.org/0000-0002-2957-8717

Viktoria Schlykow − *Peter Grünberg Institute 9 (PGI-9) and JARA-Fundamentals of Future Information Technologies (JARA-FIT), Forschungszentrum Jülich, 52425 Jülich, Germany*

Jacopo Frigerio − *LNESS Dipartimento di Fisica, Politecnico di Milano, 22100 Como, Italy*

Carlo Zucchetti − *LNESS Dipartimento di Fisica, Politecnico di Milano, 22100 Como, Italy*

Andrea De Iacovo − *Dipartimento di Ingegneria, Università Roma Tre, 00146 Rome, Italy;* orcid.org/0000-0001-5006-5505

Lorenzo Colace − *Dipartimento di Ingegneria, Università Roma Tre, 00146 Rome, Italy*

Yuji Yamamoto − *IHP − Leibniz-Institut für innovative Mikroelektronik, D-15236 Frankfurt, Oder, Germany*

Giovanni Capellini − *IHP − Leibniz-Institut für innovative Mikroelektronik, D-15236 Frankfurt, Oder, Germany; Dipartimento di Scienze, Università Roma Tre, 00146 Roma, Italy;* orcid.org/0000-0002-5169-2823

Detlev Grützmacher − *Peter Grünberg Institute 9 (PGI-9) and JARA-Fundamentals of Future Information Technologies*

https://doi.org/10.1021/acsphotonics.1c00617
ACS Photonics 2021, 8, 2166−2173

(JARA-FIT), Forschungszentrum Jülich, 52425 Jülich, Germany

Giovanni Isella − *LNESS Dipartimento di Fisica, Politecnico di Milano, 22100 Como, Italy;* orcid.org/0000-0001-5951-7440

Complete contact information is available at: https://pubs.acs.org/10.1021/acsphotonics.1c00617

Notes

The authors declare no competing financial interest.

■ ACKNOWLEDGMENTS

Part of this work has been funded by the EU Horizon-2020 Project microSPIRE ID 766955, the German Federal Ministry of Education and Research (BMBF) in frame of the M-ERA.NET Project GESNAPHOTO and ForMikro Project SiGeSn NanoFET. The authors acknowledge Andrea Barzaghi and Daniel Chrastina for their support on single-pixel imaging and X-ray diffraction measurements, respectively.

■ REFERENCES

(1) Hyperspectral Imaging Systems Market by Application and Component − 2021, Marketsandmarkets.com, 2017.

(2) García De Arquer, F. P.; Armin, A.; Meredith, P.; Sargent, E. H. Solution-Processed Semiconductors for next-Generation Photodetectors. *Nat. Rev. Mater.* **2017**, *2* (3). DOI: 10.1038/natrevmats.2016.100.

(3) Sevick-Muraca, E. M. Optical Imaging: Resolutely Deep and Fast. *Nat. Biomed. Eng.* **2017**, *1* (4), 1−3.

(4) Rajendran, S.; Sadooni, F. N.; Al-Kuwari, H. A. S.; Oleg, A.; Govil, H.; Nasir, S.; Vethamony, P. Monitoring Oil Spill in Norilsk, Russia Using Satellite Data. *Sci. Rep.* **2021**, *11* (1), 1−20.

(5) Kantamneni, H.; Zevon, M.; Donzanti, M. J.; Zhao, X.; Sheng, Y.; Barkund, S. R.; McCabe, L. H.; Banach-Petrosky, W.; Higgins, L. M.; Ganesan, S.; Riman, R. E.; Roth, C. M.; Tan, M. C.; Pierce, M. C.; Ganapathy, V.; Moghe, P. V. Surveillance Nanotechnology for Multi-Organ Cancer Metastases. *Nat. Biomed. Eng.* **2017**, *1* (12), 993−1003.

(6) Bijelic, M.; Gruber, T.; Mannan, F.; Kraus, F.; Ritter, W.; Dietmayer, K.; Heide, F. Seeing through Fog without Seeing Fog: Deep Multimodal Sensor Fusion in Unseen Adverse Weather. *Proc. IEEE Comput. Soc. Conf. Comput. Vis. Pattern Recognit.* **2020**, 11679−11689.

(7) Brown, A. S. Drones and Optical Sensors: No Longer a Remote Possibility. *Photonics Focus* **2021**, *2* (2), 22−26.

(8) González, A.; Fang, Z.; Socarras, Y.; Serrat, J.; Vázquez, D.; Xu, J.; López, A. M. Pedestrian Detection at Day/Night Time with Visible and FIR Cameras: A Comparison. *Sensors* **2016**, *16* (6), 820.

(9) Rogalski, A. *Infrared Detectors*; CRC Press, 2020.

(10) Wirths, S.; Geiger, R.; von den Driesch, N.; Mussler, G.; Stoica, T.; Mantl, S.; Ikonic, Z.; Luysberg, M.; Chiussi, S.; Hartmann, J. M.; Sigg, H.; Faist, J.; Buca, D.; Grützmacher, D. Lasing in Direct-Bandgap GeSn Alloy Grown on Si. *Nat. Photonics* **2015**, *9* (2), 88−92.

(11) Elbaz, A.; Buca, D.; von den Driesch, N.; Pantzas, K.; Patriarche, G.; Zerounian, N.; Herth, E.; Checoury, X.; Sauvage, S.; Sagnes, I.; Foti, A.; Ossikovski, R.; Hartmann, J. M.; Boeuf, F.; Ikonic, Z.; Boucaud, P.; Grützmacher, D.; El Kurdi, M. Ultra-Low-Threshold Continuous-Wave and Pulsed Lasing in Tensile-Strained GeSn Alloys. *Nat. Photonics* **2020**, *14* (6), 375−382.

(12) Zhou, Y.; Miao, Y.; Ojo, S.; Tran, H.; Abernathy, G.; Grant, J. M.; Amoah, S.; Salamo, G.; Du, W.; Liu, J.; Margetis, J.; Tolle, J.; Zhang, Y.; Sun, G.; Soref, R. A.; Li, B.; Yu, S.-Q. Electrically Injected GeSn Lasers on Si Operating up to 100 K. *Optica* **2020**, *7* (8), 924.

(13) Tran, H.; Pham, T.; Margetis, J.; Zhou, Y.; Dou, W.; Grant, P. C.; Grant, J. M.; Al-Kabi, S.; Sun, G.; Soref, R. A.; Tolle, J.; Zhang, Y.-H.; Du, W.; Li, B.; Mortazavi, M.; Yu, S.-Q. Si-Based GeSn Photodetectors toward Mid-Infrared Imaging Applications. *ACS Photonics* **2019**, *6* (11), 2807−2815.

(14) Slav, A.; Dascalescu, I.; Lepadatu, A. M.; Palade, C.; Zoita, N. C.; Stroescu, H.; Iftimie, S.; Lazanu, S.; Gartner, M.; Buca, D.; Teodorescu, V. S.; Ciurea, M. L.; Braic, M.; Stoica, T. GeSn/SiO2Multilayers by Magnetron Sputtering Deposition for Short-Wave Infrared Photonics. *ACS Appl. Mater. Interfaces* **2020**, *12* (50), 56161−56171.

(15) Slav, A.; Palade, C.; Logofatu, C.; Dascalescu, I.; Lepadatu, A. M.; Stavarache, I.; Comanescu, F.; Iftimie, S.; Antohe, S.; Lazanu, S.; Teodorescu, V. S.; Buca, D.; Ciurea, M. L.; Braic, M.; Stoica, T. GeSn Nanocrystals in GeSnSiO 2 by Magnetron Sputtering for Short-Wave Infrared Detection. *ACS Appl. Nano Mater.* **2019**, *2* (6), 3626−3635.

(16) Moutanabbir, O.; Assali, S.; Gong, X.; O'Reilly, E.; Broderick, C. A.; Marzban, B.; Witzens, J.; Du, W.; Yu, S.-Q.; Chelnokov, A.; Buca, D.; Nam, D. Monolithic Infrared Silicon Photonics: The Rise of (Si)GeSn Semiconductors. *Appl. Phys. Lett.* **2021**, *118* (11), 110502.

(17) Liu, M.; Yang, D.; Shkurmanov, A.; Bae, J. H.; Schlykow, V.; Hartmann, J.-M.; Ikonic, Z.; Baerwolf, F.; Costina, I.; Mai, A.; Knoch, J.; Grützmacher, D.; Buca, D.; Zhao, Q.-T. Epitaxial GeSn/Ge Vertical Nanowires for p-Type Field-Effect Transistors with Enhanced Performance. *ACS Appl. Nano Mater.* **2021**, *4* (1), 94−101.

(18) Campbell, J. C.; Lee, T. P.; Dentai, A. G.; Burrus, C. A. Dual-Wavelength Demultiplexing InGaAsP Photodiode. *Appl. Phys. Lett.* **1979**, *34* (6), 401−402.

(19) Haddadi, A.; Dehzangi, A.; Chevallier, R.; Adhikary, S.; Razeghi, M. Bias-Selectable NBn Dual-Band Long-/Very Long-Wavelength Infrared Photodetectors Based on InAs/InAs1-xSbx/AlAs1-xSbx Type-II Superlattices. *Sci. Rep.* **2017**, *7* (1), 3379.

(20) Rogalski, A.; Antoszewski, J.; Faraone, L. Third-Generation Infrared Photodetector Arrays. *J. Appl. Phys.* **2009**, *105* (9), 091101.

(21) Hoang, A. M.; Dehzangi, A.; Adhikary, S.; Razeghi, M. High Performance Bias-Selectable Three-Color Short-Wave/Mid-Wave/Long-Wave Infrared Photodetectors Based on Type-II InAs/GaSb/AlSb Superlattices OPEN. *Sci. Rep.* **2016**, na DOI: 10.1038/srep24144.

(22) Xie, Z.; Deng, Z.; Zou, X.; Chen, B. InP-Based Near Infrared/Extended-Short Wave Infrared Dual-Band Photodetector. *IEEE Photonics Technol. Lett.* **2020**, *32* (16), 1003−1006.

(23) Blazejewski, E. R.; Arias, J. M.; Williams, G. M.; Mclevige, W.; Zandian, M.; Pasko, J. Bias-Switchable Dual-Band HgCdTe Infrared Photodetector. *J. Vac. Sci. Technol., B: Microelectron. Process. Phenom.* **1992**, *10*, 1626.

(24) Tang, X.; Ackerman, M. M.; Chen, M.; Guyot-Sionnest, P. Dual-Band Infrared Imaging Using Stacked Colloidal Quantum Dot Photodiodes. *Nat. Photonics* **2019**, *13* (4), 277−282.

(25) Masini, G.; Colace, L.; Galluzzi, F.; Assanto, G.; Pearsall, T. P.; Presting, H. Voltage Tunable SiGe Photodetector: A Novel Tool for Crypted Optical Communications through Wavelength Mixing. *Appl. Phys. Lett.* **1997**, *70* (24), 3194−3196.

(26) Simola, E. T.; De Iacovo, A.; Frigerio, J.; Ballabio, A.; Fabbri, A.; Isella, G.; Colace, L. Voltage-Tunable Dual-Band Ge/Si Photodetector Operating in VIS and NIR Spectral Range. *Opt. Express* **2019**, *27* (6), 8529.

(27) Yamamoto, Y.; Zaumseil, P.; Arguirov, T.; Kittler, M.; Tillack, B. Low Threading Dislocation Density Ge Deposited on Si (1 0 0) Using RPCVD. *Solid-State Electron.* **2011**, *60* (1), 2−6.

(28) von den Driesch, N.; Stange, D.; Wirths, S.; Mussler, G.; Holländer, B.; Ikonic, Z.; Hartmann, J. M.; Stoica, T.; Mantl, S.; Grützmacher, D.; Buca, D. Direct Bandgap Group IV Epitaxy on Si for Laser Applications. *Chem. Mater.* **2015**, *27* (13), 4693−4702.

(29) Yamamoto, Y.; Zaumseil, P.; Schubert, M. A.; Tillack, B. Influence of Annealing Conditions on Threading Dislocation Density in Ge Deposited on Si by Reduced Pressure Chemical Vapor Deposition. *Semicond. Sci. Technol.* **2018**, *33* (12), 124007.

(30) Hishikawa, Y.; Nakamura, N.; Tsuda, S.; Nakano, S.; Kishi, Y.; Kuwano, Y. Interference-Free Determination of the Optical Absorption Coefficient and the Optical Gap of Amorphous Silicon Thin Films. *Jpn. J. Appl. Phys.* **1991**, *30* (Part 1, No. 5), 1008−1014.

(31) Michel, J.; Liu, J.; Kimerling, L. C. High-Performance Ge-on-Si Photodetectors. *Nat. Photonics* **2010**, *4* (8), 527−534.
(32) Chen, Y.; Xie, Z.; Huang, J.; Deng, Z.; Chen, B. High-Speed Uni-Traveling Carrier Photodiode for 2 Mm Wavelength Application. *Optica* **2019**, *6* (7), 884.
(33) Gaury, B.; Sun, Y.; Bermel, P.; Haney, P. M. Sesame: A 2-Dimensional Solar Cell Modeling Tool. *Sol. Energy Mater. Sol. Cells* **2019**, *198*, 53−62.
(34) Silvano, D. *Photodetectors: Devices, Circuits and Applications*, 2nd ed..; John Wiley & Sons, 2021.
(35) Tran, H.; Littlejohns, C. G.; Thomson, D. J.; Pham, T.; Ghetmiri, A.; Mosleh, A.; Margetis, J.; Tolle, J.; Mashanovich, G. Z.; Du, W.; Li, B.; Mortazavi, M.; Yu, S.-Q. Study of GeSn Mid-Infrared Photodetectors for High Frequency Applications. *Front. Mater.* **2019**, *6*, 1−7.
(36) Lee, K.-C.; Lin, M.-X.; Li, H.; Cheng, H.-H.; Sun, G.; Soref, R.; Hendrickson, J. R.; Hung, K.-M.; Scajev, P.; Medvids, A. Planar GeSn Photodiode for High-Detectivity Photodetection at 1550 Nm. *Appl. Phys. Lett.* **2020**, *117*, 012102.
(37) Cucci, C.; Casini, A. Hyperspectral Imaging for Artworks Investigation. In *Hyperspectral Imaging*; Amigo, J. M., Ed.; 2020; pp 583−604, DOI: 10.1016/B978-0-444-63977-6.00023-7.
(38) Bao, J.; Bawendi, M. G. A Colloidal Quantum Dot Spectrometer. *Nature* **2015**, *523* (7558), 67−70.

https://doi.org/10.1021/acsphotonics.1c00617
ACS Photonics 2021, 8, 2166−2173